Effect of Secondary Fluid Motion on Laminar Flow Heat Transfer in Helically Coiled Tubes

A. N. DRAVID, K. A. SMITH, E. W. MERRILL, and P. L. T. BRIAN

Department of Chemical Engineering
Massachusetts Institute of Technology, Cambridge, Massachusetts 02139

It is well known that in the case of laminar flow of a fluid through a cylindrical tube, the axis of which forms a helix of small pitch, the primary (axial) flow field is accompanied by a secondary flow field which acts in a plane perpendicular to the tube axis and which is symmetrical about the plane of curvature of the tube. In this paper the system under study is a helical coil of small pitch and small aspect ratio a/R.

Dean (*6, 7*) first showed that the parameter

$$N_{De} = N_{Re}\sqrt{a/R} \tag{1}$$

now known as the Dean number, is the unique dynamic similarity parameter governing fluid motion in such a coil. Adler (*1*), Barua (*2*), and Mori and Nakayama (*13*) have shown that at high Dean numbers ($N_{De} > 100$), the secondary flow field consists of a relatively inviscid core and a viscous boundary layer, as shown in Figure 1.

Many workers have shown that secondary flow increases heat and mass transfer rates in addition to the rate of momentum transfer, the latter resulting in an increased pressure drop. Weissman and Mockros (*17*) obtained numerical entrance region solutions which showed little enhancement in transport rates at Dean numbers less than 20. Mori and Nakayama (*13, 14*) have shown that at high Dean numbers heat transfer coefficients in the thermally fully developed region are higher in a coiled tube than in a straight tube by a factor which varies as $\sqrt{N_{De}}$. Berg and Bonilla (*3*) and Kubair and Kuloor (*10, 11*) have reported experimental data on length-averaged heat transfer coefficients as functions of Dean and Prandtl numbers. Seban and McLaughlin (*16*) attempted to measure local heat transfer coefficients in the thermal entrance region of helically coiled tubes as a function of circumferential and axial positions on the tube wall. In some experimental runs they observed cyclic oscillations of the heat transfer coefficient with increasing downstream distance, but could not account for this apparently erroneous behavior.

Thus Weissman and Mockros studied the entrance region but did not study high Dean numbers, while Mori and Nakayama studied high Dean numbers but analyzed only the fully developed temperature field. From the practical standpoint, especially in the case of fluids with high Prandtl or Schmidt numbers, the region of developing temperature field at high Dean numbers could be important, and no analysis exists in this regime. This paper therefore has two objectives: First, to study the development of the temperature field and relate it to the cyclic oscillations observed by Seban and McLaughlin; and second, to recommend design values of the heat transfer coefficients for helically coiled tubes operating in the thermal entrance region.

The results presented herein are limited to the laminar flow regime and Dean numbers above 100, with an emphasis on a fundamental understanding of the developing temperature field. For this purpose, the differential equation of heat transport has been solved in two steps: First, an analytical approximation applicable within about one tube radius from the start of the heat transfer zone, and second, the complete numerical solution covering both the entire thermal entrance region and the fully developed region. Numerical results are compared with experimental data in the range in which they overlap. More experimental data are presented to cover the range of higher Dean and Prandtl numbers.

THE EQUATION OF HEAT TRANSPORT

At small aspect ratios ($a/R << 1$) and small pitch, the cylindrical coordinate system, shown in Figure 2, is applicable with $R\psi/a = z$, the axial distance along the tube centerline. The following assumptions are introduced:

1. The aspect ratio is small.
2. Axial conduction is negligible compared with axial convection. Usually, $N_{Pe} > 20$ assures the validity of this assumption. All cases studied in this paper satisfy this condition.
3. The flow field is fully developed before heat transfer starts. In what follows, the expression tube inlet will imply the initiation of heat transfer with velocities already developed.
4. The fluid properties are constant.
5. Viscous dissipation of energy is negligible.

With these assumptions, the equation of heat transport is

$$\frac{1}{r}\frac{\partial(rv_rT)}{\partial r} + \frac{1}{r}\frac{\partial(v_\theta T)}{\partial\theta} + \frac{\partial(v_zT)}{\partial z} = \frac{1}{N_{Pr}}\left[\frac{\partial^2T}{\partial r^2} + \frac{1}{r}\frac{\partial T}{\partial r} + \frac{1}{r^2}\frac{\partial^2T}{\partial\theta^2}\right] \tag{2}$$

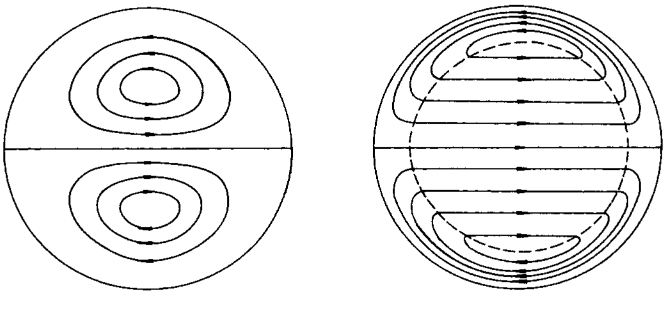

$N_{De} < 20$ $N_{De} > 100$

Fig. 1. Secondary flow field at low and high Dean numbers.

Correspondence concerning this article should be addressed to Prof. K. A. Smith at MIT, Room 12-185. A. N. Dravid is with Shell Development Co., 1400-53rd St., Emeryville, California 94608.

where v_r, v_θ and v_z are radial, circumferential and axial velocities respectively, made dimensionless by scaling them with respect to ν/a, where ν is the kinematic viscosity.

In what follows, $\theta = -\pi/2$ will be assumed to be the inside of curvature and $\theta = +\pi/2$, the outside. By assumptions (3 to 5), none of the velocities are functions of z. Mori and Nakayama (*13*) have derived the velocity field as functions of r and θ for the high Dean number regime ($N_{De} > 100$). It consists of a hydrodynamic boundary layer and a relatively inviscid inner core and is described by the following velocity components.

The core region:

$$v_r = D \sin\theta \tag{3}$$

$$v_\theta = D \cos\theta \tag{4}$$

$$v_z = A + \frac{C}{D} r \sin\theta \tag{5}$$

The boundary layer:

$$v_r = \frac{D\sin\theta}{r}\left[\left(\frac{12}{\delta}-6\right)\frac{(1-r)^2}{2\delta} + \left(9-\frac{24}{\delta}\right)\frac{(1-r)^3}{3\delta^2} + \left(\frac{12}{\delta}-4\right)\frac{(1-r)^4}{4\delta^3}\right] \tag{6}$$

$$v_\theta = -D\cos\theta\left[\left(\frac{12}{\delta}-6\right)\left(\frac{1-r}{\delta}\right) + \left(9-\frac{24}{\delta}\right)\left(\frac{1-r}{\delta}\right)^2 + \left(\frac{12}{\delta}-4\right)\left(\frac{1-r}{\delta}\right)^3\right] \tag{7}$$

$$v_z = \left[A + \frac{C}{D}(1-\delta)\sin\theta\right]\left[2\left(\frac{1-r}{\delta}\right) - \left(\frac{1-r}{\delta}\right)^2\right] + \frac{C}{D}\delta\sin\theta\left[\left(\frac{1-r}{\delta}\right) - \left(\frac{1-r}{\delta}\right)^2\right] \tag{8}$$

A, C, D, and δ are constants which are functions of N_{Re} and N_{De}.

Three wall boundary conditions are considered:

1. Constant wall temperature:

   at $r = 1$, $T = 1$, at all θ and z.

2. Constant wall heat flux:

   at $r = 1$, $\partial T/\partial r = 0.25\, N_{Re}N_{Pr}$, at all θ and z.

3. Wall heat flux varies with θ so that the wall temperature is independent of θ at any z, but the θ-averaged wall heat flux is independent of z so that dT_b/dz is constant:

   at $r = 1$, $\partial T/\partial\theta = 0$, consistent with $dT_b/dz = 1$.

Other boundary conditions common to these three cases are at $z = 0$, $T = 0$ and at $\theta = \pm\pi/2$, $\partial T/\partial\theta = 0$ (symmetry about the plane of curvature).

ASYMPTOTIC APPROXIMATION AT THE TUBE INLET

Very near the tube inlet the thermal boundary layer is very thin, and circumferential conduction and both circumferential and radial convection can be neglected compared with the radial conduction. Furthermore, it may be assumed that

$$\frac{1}{r}\frac{\partial T}{\partial r} << \frac{\partial^2 T}{\partial r^2} \tag{9}$$

so that Equation (2) reduces to

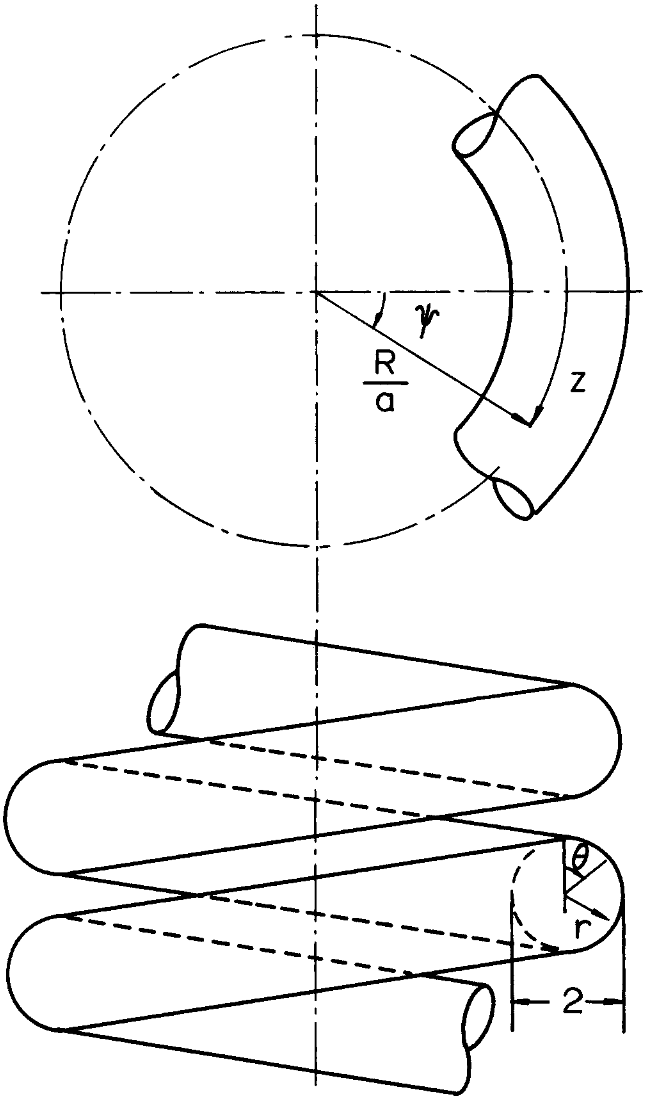

Fig. 2. Helical coordinate system. All distances are made dimensionless by scaling with respect to the tube radius a. When $a/R << 1$, the system approximates a cylindrical coordinate system.

$$v_z \frac{\partial T}{\partial z} = \frac{1}{N_{Pr}}\frac{\partial^2 T}{\partial r^2} \tag{10}$$

Near the wall, v_z can be simplified to a form varying linearly with the distance from the wall:

$$v_z = (1-r)\left[\frac{2}{\delta}\left(A + \frac{C}{D}\sin\theta\right) - \frac{C}{D}\sin\theta\right] \tag{11}$$

Equation (10) then becomes

$$(1-r)\left[\frac{2}{\delta}\left(A + \frac{C}{D}\sin\theta\right) - \frac{C}{D}\sin\theta\right]\frac{\partial T}{\partial z} = \frac{1}{N_{Pr}}\frac{\partial^2 T}{\partial r^2} \tag{12}$$

Except for the factor accounting for the circumferential variation of axial velocity, this equation can be easily recognized to be the straight tube inlet approximation of Leveque (*12*). It can be solved in the manner of Leveque to show that for any wall boundary condition, the ratio of the local heat transfer coefficient in a coiled tube to that in a straight tube, defined as the enhancement factor E, is given by

$$E = \left[\frac{1}{2N_{Re}} \left\{ \frac{2}{\delta} \left(A + \frac{C}{D} \sin\theta \right) - \frac{C}{D} \sin\theta \right\} \right]^{1/3} \tag{13}$$

This expression can be integrated with respect to θ to obtain a θ-averaged enhancement factor $\overline{E}$:

$$\overline{E} = \left(\frac{A}{\delta N_{Re}} \right)^{1/3} \left[1 - \frac{1}{18} \left\{ \frac{\delta}{2A} \left(\frac{2}{\delta} - 1 \right) \frac{C}{D} \right\}^{2} \right]$$

$$\cong 0.94 \left(\frac{A}{\delta N_{Re}} \right)^{1/3} \tag{14}$$

Substituting for A and δ using Mori and Nakayama's values

$$\overline{E} = 0.447\, {N_{De}}^{1/6} \text{ approximately.} \tag{15}$$

Equation (15) yields $\overline{E} = 1$ at $N_{De} = 125$ and $\overline{E} = 1.41$ at $N_{De} = 1{,}000$. Therefore it is seen that at very short distances from the tube inlet, the secondary flow does not improve heat transfer coefficients significantly because the temperature field has not sufficiently penetrated the secondary flow field. It must not be erroneously concluded from Equation (15) that, for $N_{De} < 125$, a coiled tube is worse than a straight tube. The reduction of Equation (14) to Equation (15) involves more restrictions on the value of N_{De} than does Mori and Nakayama's hydrodynamic analysis, making Equation (15) invalid for Dean numbers less than about 200.

There are two constraints on the applicability of the inlet approximation: First, the assumption of the linear variation of v_z with $(1 - r)$, and second, the assumption involved in neglecting certain terms of Equation (2). It has been found for the present range of N_{De} and N_{Pr} that the second constraint breaks down at a smaller axial distance than the first. Furthermore, this distance decreases with increasing Dean number, that is, with increasing secondary convection. For a typical case of $N_{De} = 225$, the ratio of circumferential to axial convection at $\theta = 0$ has been calculated as a function of r and z from the inlet solution, and its maximum value reaches 0.3 at $z = 1$. For this case, therefore, the inlet approximation should be valid only within approximately $z = 1$, which corresponds to a downstream distance equal to about one tube radius. A complete numerical solution for this case, discussed later, does indeed show this to be the case. Also, numerical results indicate that the Leveque length is relatively insensitive to N_{Pr}, in contrast with the Leveque length for a straight tube which depends strongly on N_{Pr}.

THE COMPLETE NUMERICAL SOLUTION

To describe the region beyond the Leveque length, Equation (2) must be solved with appropriate boundary conditions. Peaceman and Rachford (*15*) have proposed an alternating-direction-implicit (ADI) finite-difference technique for the two-dimensional unsteady state heat conduction problem. This technique retains the accuracy of the well-known Crank-Nicolson procedure (*5*), but simplifies the computations, using a two-step procedure, each step involving temperatures implicit in a single direction. Since the term z/v_z is analogous to the axial residence time, the present problem is similar to the unsteady state heat conduction problem in two dimensions. Thus, in the present case, z was treated like time in the Peaceman-Rachford procedure. The finite-difference equations were written in a slightly modified but equivalent form in the manner of Brian (*4*).

The procedure consists of three iterations at a given axial distance increment Δz. The entire temperature field at the previous axial distance z is known. The first two of these three iterations compute two sets of temperature values at all points of the $r - \theta$ grid at a fractional axial increment $\epsilon\Delta z$. The first set is smoothed in r direction while the second one is smoothed in θ direction. The third iteration computes the final temperatures at the fully advanced axial distance $z + \Delta z$. These three iterations are repeated for each subsequent increment in the z direction.

Thus, indicating the known temperatures at the n^{th} z increment (at distance z) by T_n and the unknown temperatures at distance $(z + \epsilon\Delta z)$ by T^*, one can write Equation (2) as

$$\Delta_r{}^2 T^* + \frac{1}{r} \Delta_r{}^1 \left(T^* - r v_r N_{Pr} T^* \right) + \frac{1}{r^2} \Delta_\theta{}^2 T_n$$

$$- \frac{N_{Pr}}{r} \Delta_\theta{}^1 \left(v_\theta T_n \right) = N_{Pr} v_z \left[\frac{T^* - T_n}{\epsilon \Delta z} \right] \tag{16}$$

This equation, along with two boundary conditions, generates a set of I tridiagonal equations in I T^* values where $(I - 1)$ is the number of radial increments from $r = 0$ to $r = 1$. Using a tridiagonal algorithm, one can determine all T^* values. This procedure is repeated along each radial line of the grid.

In the second iteration, the θ derivatives are written in terms of new unknown temperatures T^{**} at the same axial distance $z + \epsilon\Delta z$:

$$\Delta_r{}^2 T^* + \frac{1}{r} \Delta_r{}^1 \left(T^* - r v_r N_{Pr} T^* \right) + \frac{1}{r^2} \Delta_\theta{}^2 T^{**}$$

$$- \frac{N_{Pr}}{r} \Delta_\theta{}^1 \left(v_\theta T^{**} \right) = N_{Pr} v_z \left[\frac{T^{**} - T_n}{\epsilon \Delta z} \right] \tag{17}$$

Again, from these equations, T^{**} values can be determined along each circumferential line of the grid.

In the third iteration, r and θ derivatives are written in terms of known T^* and T^{**} values, respectively, while the z derivative is written in terms of the final unknown temperature T_{n+1} at the full axial increment Δz:

$$\Delta_r{}^2 T^* + \frac{1}{r} \Delta_r{}^1 \left(T^* - r v_r N_{Pr} T^* \right) + \frac{1}{r^2} \Delta_\theta{}^2 T^{**}$$

$$- \frac{N_{Pr}}{r} \Delta_\theta{}^1 \left(v_\theta T^{**} \right) = N_{Pr} v_z \left[\frac{T_{n+1} - T_n}{\Delta z} \right] \tag{18}$$

Equations (16) through (18) can be manipulated to eliminate T^{**} and the following equation results:

$$\frac{1}{r^2} \Delta_\theta{}^2 \left(T_{n+1} - T_n \right) - \frac{N_{Pr}}{r} \Delta_\theta{}^1 \left(v_\theta T_{n+1} - v_\theta T_n \right)$$

$$= N_{Pr} v_z \left[\frac{\epsilon T_{n+1} + (1 - \epsilon)\, T_n - T^*}{\epsilon^2 \Delta z} \right] \tag{19}$$

Thus use of the tridiagonal algorithm yields T^* and T_{n+1} values from Equations (16) and (19), respectively, generating the temperature field at each advanced cross section of the tube. In the present work, ϵ was assigned a value of 0.5.

Three wall boundary conditions, stated earlier, have been studied. The conditions of constant wall temperature and constant wall heat flux are often employed in the literature as reference cases. The third boundary condition, hereafter referred to as the case of isothermal periphery with axially constant wall heat flux, approximates the present experimental setup in which the circumferential conduction in the tube wall essentially eliminated the circumferential variations in the wall temperature, although the total heat flux at any cross section was independent of the axial distance. The numerical solution for

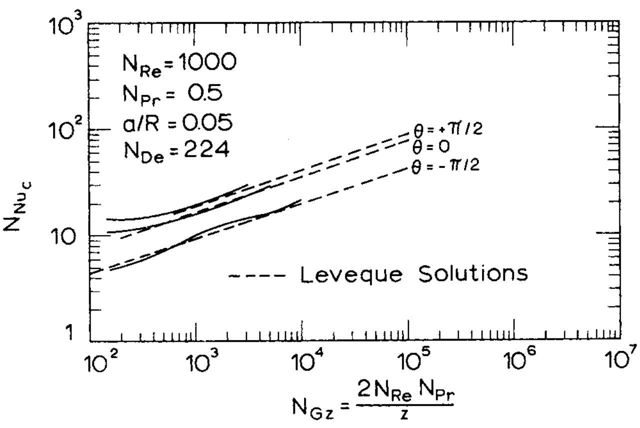

Fig. 3. Comparison between analytical and numerical results for the constant wall heat flux case. Broken lines are solutions given by Equation (13), while smooth curves represent numerical solutions.

this case involved an iterative procedure designed to find the correct wall temperature at each axial position which resulted in a linearly increasing bulk temperature.

Stability of the numerical solutions depended strongly on the relative sizes of the axial, radial, and circumferential steps, and, where unstable, the solutions exhibited rapidly growing oscillations with increasing axial distance. The solutions reported in this paper were stable and convergent. The convergence was tested by studying the effect of varying all three space increments, especially the axial increment. For instance, with $N_{Re} = 1{,}000$, $N_{Pr} = 5$, and $a/R = 0.05$, it was found that further reductions in Δr, $\Delta\theta$, and Δz by factors of 1.5, 2, and 2, respectively, had practically no effect upon the solution, irrespective of whether these reductions were made singly or jointly. It is necessary to point out here that the damping axial oscillations of the solutions reported in this paper persisted identically in the convergence tests, supporting the assertion made later that they reveal a real effect rather than any numerical instability.

A grid with 50 steps in the radial direction and 18 in the θ direction (covering the range $\theta = -\pi/2$ to $\theta = +\pi/2$) was found to be convergent within 1% with respect to both directions for $N_{Re} \cdot N_{Pr} < 5{,}000$, but the convergence became progressively poorer as $N_{Re} \cdot N_{Pr}$ increased beyond 5,000. Details of the numerical solution are given elsewhere (8).

EXPERIMENTAL PROCEDURE

Extra heavy copper tubing, 0.54 in. O.D. and 0.29 in. I.D., was used. Teflon-insulated nichrome resistance wire (25 gauge) was first wound around the tubing in a helically cut groove with a spacing of 0.2 in. The straight tube was then filled with Wood's metal to make it more resistant to distortion and wound into a helical coil with 5.4 in. diam. measured between diametrically opposite tube centerlines, providing an aspect ratio of 0.0536. The Wood's metal was removed by flushing with boiling water. The distortion of the circular cross section of the tube during bending was measured by sectioning a prototype and found to be less than 0.5%. The nichrome wire, initially of a total resistance of 120 ohms, was broken at two points to form three segments of 40 ohms each, which were connected in a delta to form a balanced, delta-connected three-phase resistive load. An initial length equivalent to 50 tube diameters was free of the heating wire and provided a calming length for the development of the velocity field. Power was supplied through a three-phase autotransformer via a wattmeter. Chromel-constantan thermocouples were soldered on the outside of the tube wall at the $\theta = 0$ positions at 17 axial positions with axially increasing spacing. At four of these stations, thermocouples were also soldered at $\theta = \pm\,\pi/2$ positions. The thermocouple leads were connected to a rotary switch via microconnectors and extension wires, all made of the thermocouple materials. The single output from the rotary switch was fed to a potentiometric recorder. The entire length of the tube was wrapped with asbestos tape and the whole assembly placed in a box which was then filled with Santocel-A insulation powder.

The flow system consisted of a feed tank, a constant-temperature bath, a pump, and a microregulating valve, all in series before the coil. Thermocouples were inserted in the fluid at the upstream and downstream locations to measure inlet and outlet temperatures. The flow rate was measured with a graduated cylinder and a microtimer.

In order to minimize the effect of a change in physical properties with temperature, the difference between the wall and bulk temperatures or between the inlet and outlet temperatures was kept below 15°C. in most runs and below 20°C. in all runs. Calculations showed that the effects of gravity and natural convection were negligible. The maximum error due to heat loss through the insulation is estimated at 3%. The temperature drop across the tube wall was negligible compared with the drop between the wall and bulk temperatures. The maximum axial deviation of the wall heat flux was less than 1%. The large thickness and high thermal conductivity of the tube wall allowed heat to conduct circumferentially within the wall. Therefore, although the heat transfer coefficient to the fluid varied over twofold around the periphery, calculations indicate that the circumferential variation in the wall temperature was negligible (that is, less than 0.1°C.), as later confirmed by the thermocouples located at the $\theta = \pm\,\pi/2$ positions.

RESULTS AND DISCUSSION

Numerical Results

Figure 3 shows the variation of the local Nusselt number with Graetz number at fixed N_{Re} and N_{Pr} for the case of constant wall heat flux. The straight lines are analytical Leveque solutions for three angular positions on the tube circumference as indicated. The agreement between the analytical and numerical solutions is excellent. Furthermore, as mentioned earlier, the Leveque length should be limited to z of the order of unity (that is, $N_{Gz} = 1{,}000$). The numerical solutions for $\theta = 0$ and $\theta = +\pi/2$ start deviating from the analytical approximations at $N_{Gz} = 700$

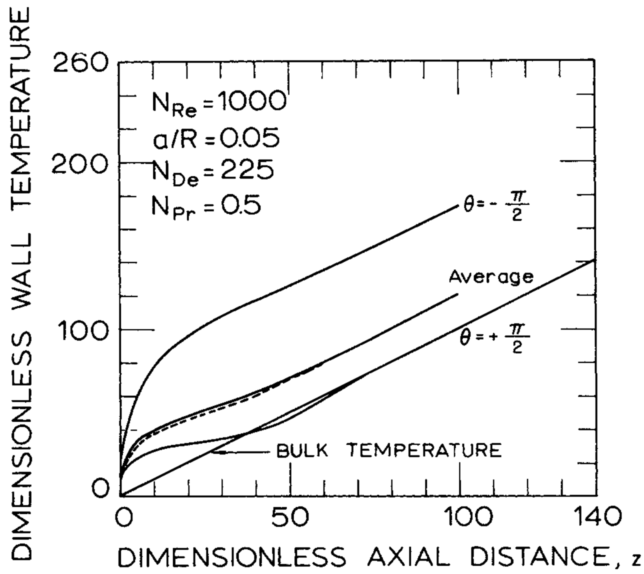

Fig. 4. Axial profiles of wall temperature at $N_{Pr} = 0.5$, computed numerically. Solid curves correspond to the case of constant wall heat flux. Broken curve corresponds to the case of isothermal periphery with axially constant wall heat flux.

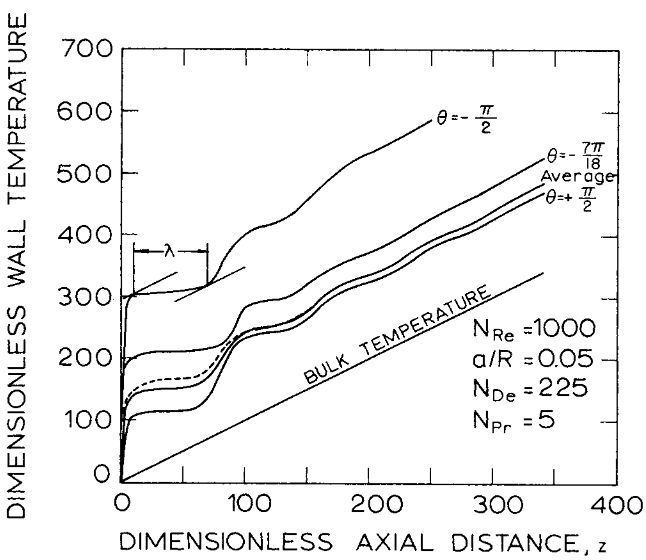

Fig. 5. Axial profiles of wall temperature at $N_{Pr} = 5$, computed numerically. Solid and broken curves have the same significance as in Figure 4. The wavelength of the first oscillation λ has been schematically defined.

and 1,000, respectively. The agreement between the analytical and numerical solutions within the range of validity of the analytical solution can also be seen in Figure 11.

Figures 4 through 6 show the axial variation of the wall temperature at several values of θ for the case of constant wall heat flux at three values of N_{Pr}. In each case, the θ-averaged wall temperature is also plotted for a convenient comparison. The broken lines show the result for the case of isothermal periphery with axially constant wall heat flux. Figure 7 shows the axial variation of dT_b/dz for the case of constant wall temperature, the term dT_b/dz being proportional to the θ-averaged wall heat flux at any value of z.

Figures 4 through 7 display a startling characteristic feature: the axial temperature or heat flux profiles show large amplitude oscillations which decay and damp out in the fully developed region. In Figures 4 through 6 the achievement of the fully developed temperature field is indicated by the wall temperatures rising steadily parallel to the linearly climbing bulk temperature. Since the feature of the cyclic axial oscillations is common to all three boundary conditions, it must be a result of the fluid mechanics of the system. Clearly, secondary flow is the cause of this phenomenon.

For very short distances from the tube inlet, the development of the temperature field in a coiled tube is similar to that in a straight tube except for the effect of the skewed axial velocity profile, which is to set up a circumferential temperature gradient. This is the Leveque region described earlier. In this region, the thermal boundary layer is very thin, and its penetration into the secondary flow field is insufficient for the effect of the latter to become significant. However, v_r and v_θ increase as the cube and square, respectively, of the distance from the tube wall. This means that the secondary velocities increase very rapidly with increasing distance from the tube wall. Therefore, as the thermal boundary layer grows with advancing axial distance, the secondary convection of heat becomes pronounced in a short distance downstream from the Leveque region. This temporarily arrests the growth of the thermal boundary layer, with secondary convection then transferring most of the heat into the fluid core. A schematic diagram depicting this effect is shown in Figure 8. The region outside the thermal boundary layer is idealized as being at the initial temperature $T = 0$. At all points at the edge of the thermal boundary layer, the term $\frac{1}{r}\left[\frac{\partial(r v_r T)}{\partial r} + \frac{\partial(v_\theta T)}{\partial \theta}\right]$ has become very large, which means that heat is convected very fast circumferentially and then transferred into the core as the circumferential streamline is converted into a radial streamline entering the fluid core at A. It is to be noted that the other core streamlines lying above the streamline AB can still be idealized as being at $T = 0$, because they are the continuations of those circumferential streamlines which lie outside the thermal boundary layer.

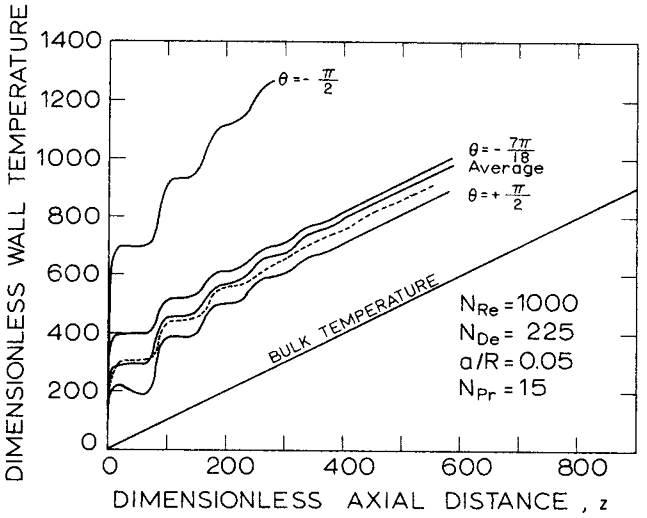

Fig. 6. Axial profiles of wall temperature at $N_{Pr} = 15$, computed numerically. Solid and broken curves have the same significance as in Figure 4.

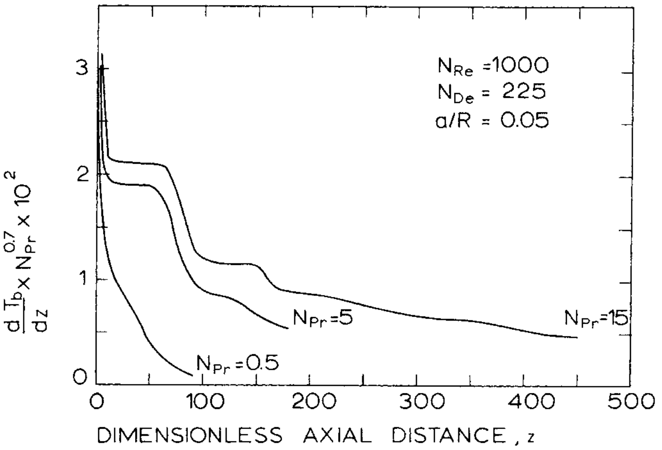

Fig. 7. Axial profiles of the θ-averaged wall heat flux at several values of N_{Pr}, computed numerically. The term dT_b/dz is proportional to the θ-averaged wall heat flux.

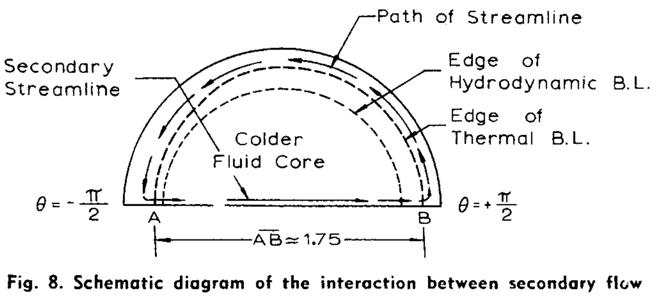

Fig. 8. Schematic diagram of the interaction between secondary flow and propagating thermal boundary layer.

As the first hot fluid element enters the fluid core at A, it ideally generates a step change in temperature which propagates from A to B with velocity v_{r_0}. During this interval, the thermal boundary layer merely transmits most of the heat, and temperatures in the thermal boundary layer do not increase substantially because heat is rapidly convected away from its outer edge. This corresponds to the flat region in the axial temperature profile shown in Figures 4 through 6. When the propagating step change encounters the thermal boundary layer at B and then propagates circumferentially, the temperature at the outer edge of the thermal boundary layer is suddenly increased. This results in a sharp decline in the rate of convective heat transfer from the edge of the thermal boundary layer to the core. Therefore the temperatures in the thermal boundary layer rise rapidly once again with increasing downstream distance. This interaction between secondary flow and heat transfer accounts for the first cycle in the oscillations shown in Figures 4 through 7. It is suspected that the second and subsequent oscillations are resonances of the first one, but their analysis becomes excessively complex because of the rapidly growing complexity of the temperature field.

Figures 9a through 9e show the numerically computed development of the temperature field, which is consistent with the above description. At five different axial positions, the temperature field has been plotted in the form of isotherms at various temperature levels. The wall boundary condition is that of constant wall heat flux, but the results for other boundary conditions are similar. A conventional thermal boundary layer is seen at $z = 1.5$. It is skewed because of the skewed axial velocity profile. At $z = 10$, each isotherm becomes kidney-shaped, and between $z = 10$ and $z = 80$, the concave portions of the kidneys transform into long horizontal spikes penetrating the fluid core, whereas the temperatures in the region near the wall do not increase substantially. This, then, is the region of relatively constant ordinate between $z = 10$ and $z = 65$ in Figures 4 through 7, in which the thermal boundary layer merely transmits most of the heat from the wall to the core without absorbing much of it. The plot for $z = 300$ is the fully developed temperature field. It shows that in the relatively colder region, the isotherms have separated into two closed contours symmetrical about the plane of curvature of the coil. Finally, it is interesting to note that the coldest point in the tube cross section shifts from $\theta = +\pi/2$ to some position between $\theta = 0$ and $\theta = +\pi/2$, in contradiction to the general belief (*16*) that $\theta = +\pi/2$ corresponds to the coldest point at all axial positions.

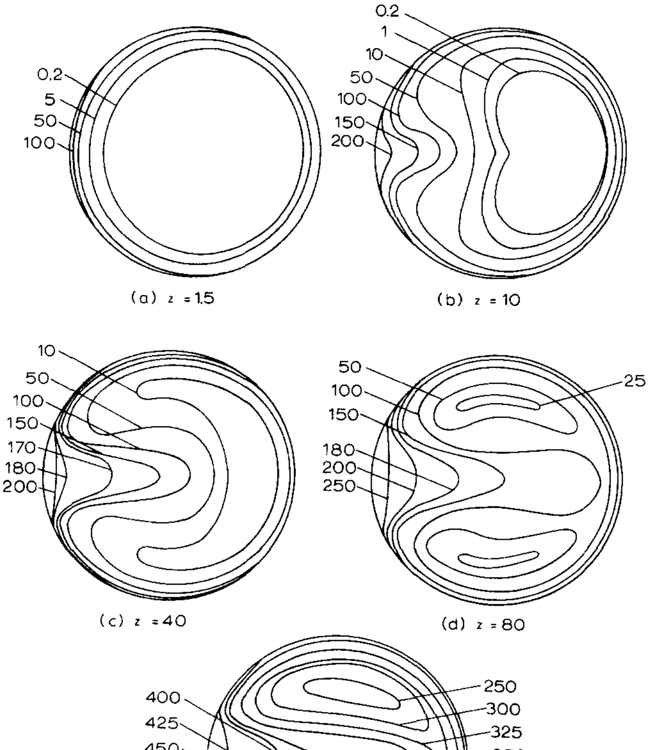

(a) $z = 1.5$ (b) $z = 10$ (c) $z = 40$ (d) $z = 80$ (e) $z = 300$

Fig. 9. Development of the temperature field for the constant wall heat flux case, computed numerically. Five cross sections at five axial positions are shown. Each contour represents an isotherm at the indicated dimensionless temperature. Other parameters are N_{Re} = 1,000, N_{Pr} = 5, N_{De} = 225, a/R = 0.05.

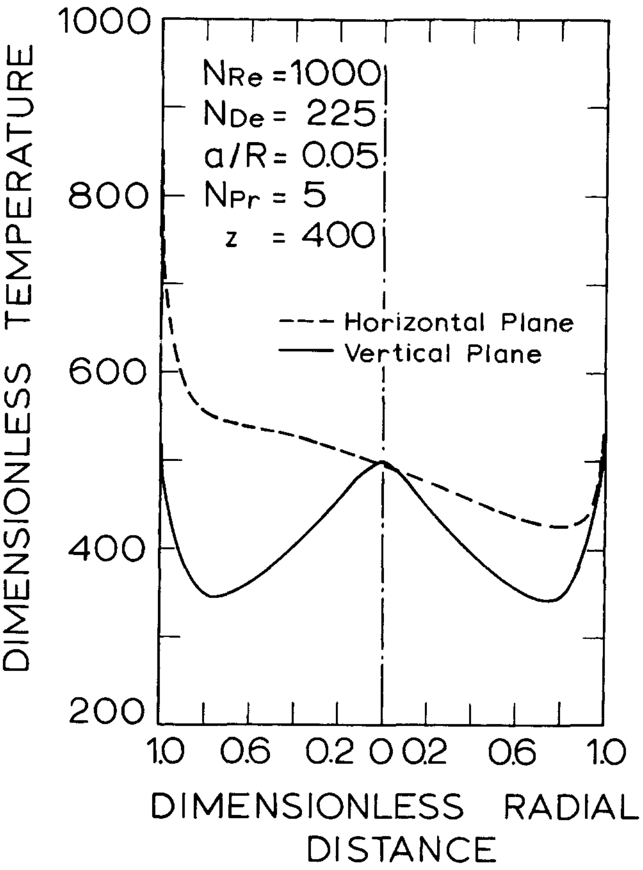

Fig. 10. Fully developed radial temperature profiles, computed numerically for the case of constant wall heat flux. The horizontal plane is the plane of curvature of the coiled tube.

These phenomena give rise to very peculiar temperature profiles in the fully developed region, which are typical of all three wall boundary conditions. Figure 10 shows the numerically computed radial temperature profiles in the horizontal and vertical planes, the horizontal plane being the plane of curvature. It is necessary to recall our assumption that flow is fully developed at the initiation of heat transfer. In practice, this simplified description fits high Prandtl number fluids quite well because their thermal entrance length is much larger than their fluid mechanical entrance length.

A few quantitative tests can be made to substantiate the arguments presented above. For this purpose, it is convenient to define a dimensionless wavelength λ of the first oscillation in Figures 4 through 6, as the dimensionless

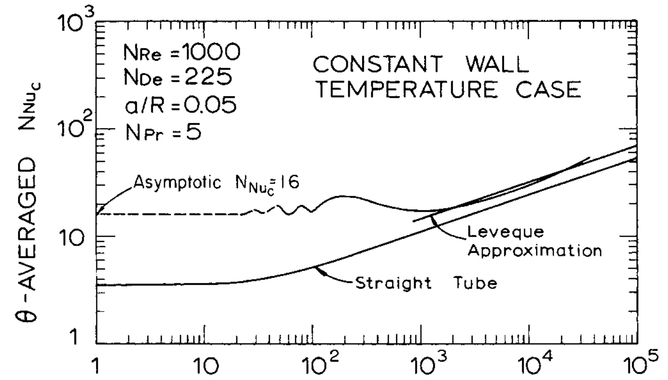

Fig. 11. Cyclic variation of local θ-averaged Nusselt number with increasing axial distance (numerical data).

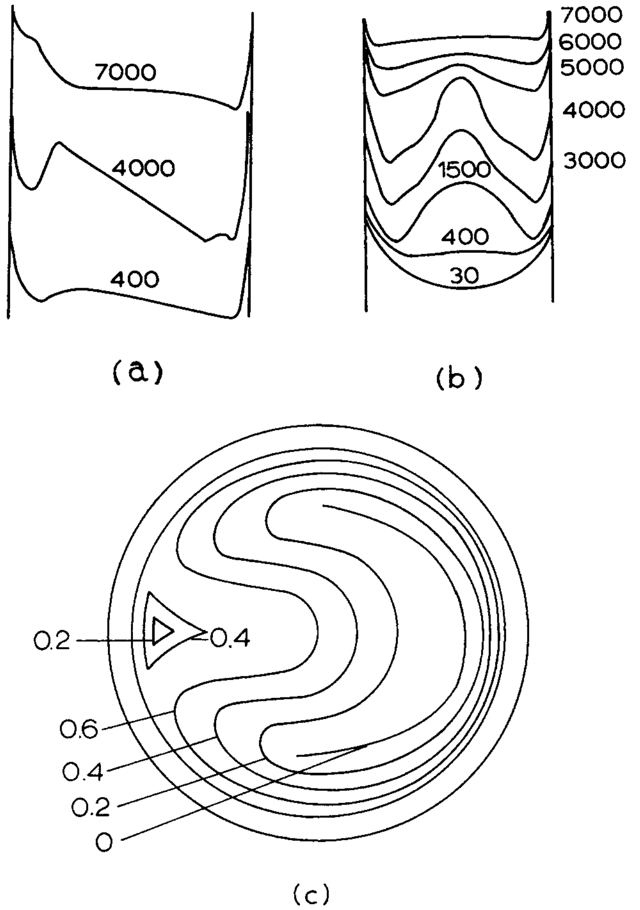

(a)

(b)

(c)

Fig. 12. Radial temperature profiles observed by Hawes *(9)*. *(a)* Horizontal plane, the parameter being N_{Re}. *(b)* Vertical plane, the parameter being N_{Re}. *(c)* Complete temperature field, drawn by extrapolating the data from *a* and *b* at N_{De} = 1,000. The parameter is the temperature (°C.) above a base value.

TABLE 1. VARIATION OF λ WITH N_{Re} AND a/R AT $N_{Pr} = 5$

a/R	N_{Re}	N_{De}	$\bar{v}_z/v_{r_0}$	λ (predicted)	λ (observed)
0.05	1,000	225	31.08	52.5	52.5
0.05	2,000	447	45.31	76.5	75.0
0.05	3,500	783	61.05	103.1	100.0
0.01	1,000	100	43.56	73.5	77.5

distance between the points at which a line parallel to the bulk temperature line is tangent to the first maximum and the first minimum in the wall temperature curve. (The procedure is illustrated in Figure 5.) This wavelength seems to be insensitive to the Prandtl number in the limited range of Prandtl numbers studied (0.5 to 15). This fact is consistent with the fact that the distance *AB* in Figure 8 is a rather weak function of N_{Pr} and that fluid mechanics alone is responsible for the secondary transport of fluid elements in relation to their bulk motion. Extending this criterion further, one can predict the wavelength of the first oscillation as a function of N_{Re} and a/R, the two parameters which determine completely the fluid mechanics of the system. Thus λ should equal the axial distance traversed by a fluid element moving with average velocity $\bar{v}_z$ in the time required for the same element to move from *A* to *B* with velocity v_{r_0}. As mentioned earlier, the latter distance is a weak function of N_{Pr}, and for the case considered ($N_{Pr} = 5$), it equals about 1.75 tube radii at $z = 10$. Furthermore, from the analysis of Mori and Nakayama (*13*)

$$\bar{v}_z = 0.5\, N_{Re} \tag{20}$$

and

$$v_{r_0} \cong 0.9656\sqrt{N_{De}} + 1.6500 \tag{21}$$

Hence

$$\lambda = 1.75\ (\bar{v}_z/v_{r_0}) \tag{22a}$$

$$= 1.75\left[\frac{0.5\, N_{Re}}{1.6500 + 0.9656\sqrt{N_{Re}}\,\sqrt[4]{a/R}}\right] \tag{22b}$$

which shows that λ should increase with increasing N_{Re} and decreasing a/R. Numerical results summarized in Table 1 verify these predictions.

Since the relative rate of heat transport by secondary convection compared with that by conduction increases with increasing N_{De} and N_{Pr}, the intensity of the cyclic behavior (measured by the amplitude of the waves) must increase with increasing N_{De} and N_{Pr}, as verified by the results presented above. Physically, $N_{Pr} = 0.5$ curve of Figure 7 is typical of gases, while $N_{Pr} = 15$ approximately represents oils.

One direct consequence of the phenomenon of the cyclically varying wall temperature or wall heat flux is a cyclically varying local Nusselt number based on the difference between the wall and bulk temperatures. The cyclic variations damp out as the fully developed temperature field is approached, and the Nusselt number approaches an asymptotic value as seen in Figure 11. According to Mori and Nakayama's analysis, this steady asymptotic value should increase with $\sqrt{N_{De}}$. The Nusselt number in the Leveque region increases only as $N_{De}{}^{1/6}$. Therefore, in comparison with straight tubes, an early asymptotic behavior of the local Nusselt number is expected, even though the Nusselt number undergoes cyclic variations because of the developing temperature field.

Comparison Between Numerical and Experimental Results

Figure 12 shows the radial temperature profiles observed experimentally by Hawes (*9*) in a coil of aspect ratio 0.1 for water ($N_{Pr} = 5$). Unfortunately, Hawes has reported no quantitative data, but the shapes of his temperature profiles are in excellent agreement with the curves in Figure 10. Figure 12*c* was constructed by Hawes using the data of Figures 12*a* and 12*b*. This plot shows the approximate shape of isotherms, and is in excellent qualitative agreement with Figure 9*c*.

Figure 13 shows the computer solution for $N_{De} = 225$ and $N_{Pr} = 5$ for the case of isothermal periphery with axially constant wall heat flux, represented by the broken line. The experimental results, represented by the solid line, correspond to the same N_{De} and N_{Pr} evaluated at the mean of the inlet and outlet temperatures. The amplitude of the waves in the experimental curve is less than that in the theoretical curve. Although this is suspected to be related to the variation of fluid properties with temperature, no conclusive explanation has been obtained for this discrepancy.

Experimental Results

A practically useful form of presenting experimental data is a plot of the local Nusselt number as a function of N_{Gz}, N_{De}, and N_{Pr}. Figure 14 shows the data for water ($N_{Pr} = 5$). The characteristic cyclic behavior is similar to that noticed by Seban and McLaughlin (*16*), who could not account for it. The straight tube Graetz solution for the case of constant wall heat flux has been plotted for comparison. An early asymptotic behavior of the local Nusselt number, also reported by Seban and McLaughlin, is apparent, although the oscillations have not decayed at the end of the tube. The asymptotic values of the Nusselt numbers are seen to increase with N_{De}. Similar data have also been obtained for four other fluids: *n*-amyl acetate ($N_{Pr} = 15$), *n*-butanol ($N_{Pr} = 35$), *n*-amyl alcohol ($N_{Pr} = 55$), and ethylene glycol ($N_{Pr} = 175$), the Prandtl numbers being based on the mean of the inlet and outlet temperatures. The complete data are presented elsewhere (*8*).

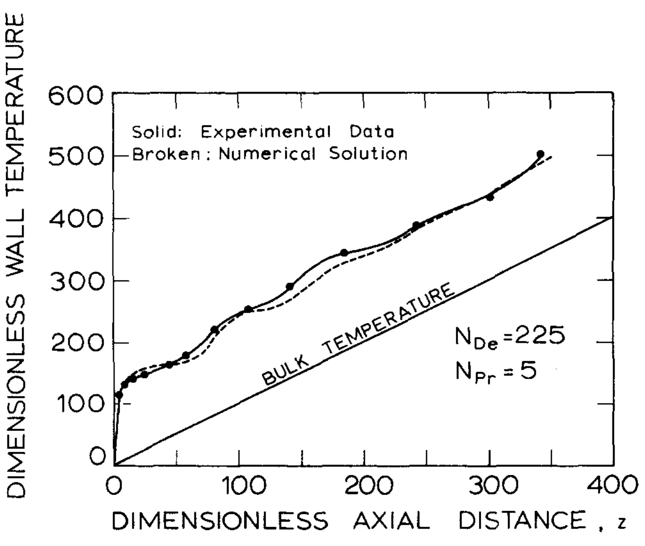

Fig. 13. Comparison between experimental and numerical results.

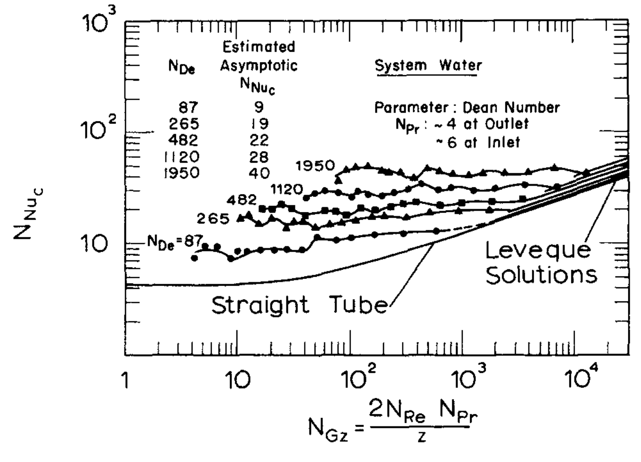

Fig. 14. Variation of the local Nusselt number with axial distance observed experimentally for water at various Dean numbers. The analytical Leveque solutions and the straight tube Graetz solution are shown for comparison.

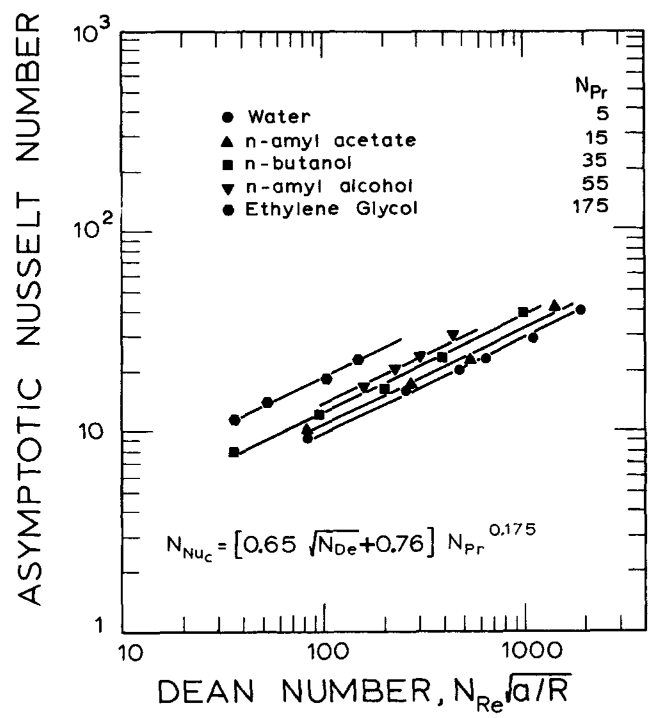

Fig. 15. Correlation of experimental data.

In view of the extremely short Leveque region and the early asymptotic behavior, it is good practice, from the point of view of design, to use a correlation based on the asymptotic heat transfer coefficient for any length of the coiled tube. Since the region of very high heat transfer coefficients (the Leveque region) is very short, such a design would be only slightly conservative. Figure 15 is a plot of the asymptotic Nusselt number as a function of N_{De} and N_{Pr}. The data points are plotted from estimated values of the fully developed Nusselt numbers such as those indicated on Figure 14. It may be recalled that the straight tube asymptotic Nusselt number is 3.66 for the constant wall temperature case and 4.36 for the constant wall heat flux case. Secondary flow is thus seen to increase these values considerably. The 0.5 power dependence on the Dean number is consistent with the analysis of Mori and Nakayama (*13*).

It is believed that Mori and Nakayama's Prandtl number dependence is incorrect. For the case $N_{Pr} > 1$, they have integrated the energy integrals of the thermal boundary-layer analysis over the hydrodynamic boundary layer rather than over the thermal boundary layer. According to their analysis, the asymptotic Nusselt numbers quickly (that is, for $N_{Pr} > 15$) reach an asymptotic limit with increasing N_{Pr}. Furthermore, their core solution is invalid for high N_{Pr}, and therefore does not predict the temperature profiles shown in Figure 10, which are supported experimentally by Hawes (*9*). Although an attempt to correct these errors leads to a rather cumbersome algebraic analysis, this analysis can be simplified in the asymptotic case of $N_{Pr} \to \infty$ to show that the asymptotic Nusselt number does not become independent of N_{Pr} as $N_{Pr} \to \infty$, but is always a continuously increasing function.

Based on the data of Figure 15, the following correlation is proposed for the asymptotic Nusselt numbers, applicable for Dean numbers between 50 and 2,000 and for Prandtl numbers between 5 and 175:

$$N_{Nu_c} = [0.76 + 0.65\sqrt{N_{De}}]\,N_{Pr}^{0.175} \qquad (23)$$

The standard deviation from this correlation was found to be 6% while the maximum deviation was 14%.

CONCLUSIONS

When a fluid flows in a helically coiled tube, centrifugal forces cause secondary fluid motion which gives rise to increased heat transfer rates. At very short distances from the start of the heat transfer zone, the thermal boundary layer is too thin to be affected by the secondary flow field, which reaches its maximum intensity at some distance away from the tube wall. Therefore near the tube inlet the ratio of heat transfer coefficient in a coiled tube to that in a straight tube (the enhancement factor) varies only as $N_{De}^{1/6}$, and a coiled tube offers little advantage over a straight tube.

For greater axial distances, the enhancement factor increases progressively and reaches a $N_{De}^{1/2}$ dependence in the fully developed region. However, the local heat transfer coefficient does not decrease continuously with axial distance, but undergoes cyclic oscillations with increasing axial distance. These oscillations damp out as the region of fully developed temperature field is approached. The oscillations arise because of the fact that even at high Dean numbers the fluid core is not well-mixed. As a result, the convective propagation of a temperature change through the core involves definite time delays.

The transition from $N_{De}^{1/6}$ dependence of the factor of enhancement at the tube inlet to the $N_{De}^{1/2}$ dependence in the fully developed region implies an early asymptotic behavior of the local Nusselt number with increasing axial distance. Since the region of $N_{De}^{1/6}$ dependence is very short compared with the entire thermal entrance region, it is recommended that the entrance effects be neglected. This would make the design only slightly conservative. Equation (23) is the recommended correlation.

ACKNOWLEDGMENT

The work presented in this paper was carried out with the partial support of U.S. Public Health Service Contract No. 43-66-491 as a part of the Artificial Kidney-Chronic Uremia Program. The numerical computations were carried out with the use of IBM 360 computer at the Information Processing Center of the Massachusetts Institute of Technology, Cambridge, Massachusetts.

NOTATION

a = tube radius, cm.
A = known function of N_{Re} and δ, $= [0.5N_{Re}]/[1 - (2/3)\delta + (1/6)\delta^2]$
C = known function of N_{Re} and δ, $= [2N_{Re}/\delta]/[1 - (2/3)\delta + (1/6)\delta^2]$
C_p = specific heat, cal./(g.) (°C.)
D = known function of N_{De}, $= 0.9656\sqrt{N_{De}} + 1.6500$
E = enhancement factor, N_{Nu_c}/N_{Nu_s}
h = heat transfer coefficient, cal./(sec.) (sq.cm.) (°C.)
k = thermal conductivity, cal./(sec.) (cm.) (°C.)
N_{De} = Dean number, $N_{Re}\sqrt{a/R}$
N_{Gz} = Graetz number, $2N_{Re}N_{Pr}/z$
N_{Nu} = Nusselt number, $2ha/k$
N_{Pe} = Peclet number, $N_{Re}N_{Pr}$
N_{Pr} = Prandtl number, $C_p\mu/k$
N_{Re} = Reynolds number, $2\,\overline{v}_z$
r = dimensionless radial distance $= \dfrac{\text{radial distance from tube centerline}}{\text{tube radius}}$
R = radius of curvature of the coil, cm.
t = temperature, °C.
T = dimensionless temperature
$= \dfrac{t - t_{\text{inlet}}}{t_w - t_{\text{inlet}}}$ (for wall boundary condition 1)
$= \dfrac{t - t_{\text{inlet}}}{dt_b/dz}$ (for wall boundary conditions 2 and 3)
v = dimensionless velocity
z = dimensionless axial distance $= \dfrac{\text{axial distance downstream from tube inlet}}{\text{tube radius}}$

Greek Letters

δ = dimensionless hydrodynamic boundary-layer thickness $= \dfrac{4.63}{\sqrt{N_{De}}} - \dfrac{0.766}{N_{De}}$
δ_T = dimensionless thermal boundary-layer thickness
Δ = finite-difference increment
Δ^1 = finite-difference equivalent of first derivative
Δ^2 = finite-difference equivalent of second derivative
ϵ = fraction determining a part of full axial increment
θ = polar angle in radians
λ = dimensionless wavelength
μ = viscosity, poise
ν = kinematic viscosity, sq.cm./sec.
ψ = azimuthal angle in radians

Subscripts

b = bulk (cup-mixed) value
c = coiled tube
n = index of axial distance step
o = tube center
r = radial direction
s = straight tube
w = value at the inside of the tube wall
z = axial direction
θ = circumferential direction

Superscripts

— = average value
$*$ = values after first iteration
$**$ = values after second iteration

LITERATURE CITED

1. Adler, M., *Z. Angew. Math. Mech.*, **14**, 257 (1934).
2. Barua, S. N., *Q. J. Mech. Appl. Math.*, **41**, Pt. 1, 61 (1963).
3. Berg, R. R., and C. F. Bonilla, *Trans. N. Y. Acad. Sci.*, Ser. II, **13**, 12 (1950).
4. Brian, P. L. T., *AIChE J.*, **7**, 367 (1961).
5. Crank, J., and P. Nicolson, *Proc. Cambridge Phil. Soc.*, **43**, 50 (1947).
6. Dean, W. R., *Phil. Mag.*, **4**, 208 (1927).
7. *Ibid.*, **5**, 673 (1928).
8. Dravid, A. N., Sc.D. thesis, Massachusetts Inst. Techn., Cambridge, Mass. (1969).
9. Hawes, W. B., *Trans. Institution Chem. Eng.*, **10**, 162 (1932).
10. Kubair, V., and N. R. Kuloor, *Ind. J. Technol.*, **3**, 147 (1965).
11. *Ibid.*, **1**.
12. Leveque, M. A., *Ann. Mines*, **13**, 201 (1928).
13. Mori, Y., and W. Nakayama, *Intern. J. Heat Mass Transfer*, **8**, 67 (1965).
14. *Ibid.*, **10**, 681 (1967).
15. Peaceman, D. W., and H. H. Rachford, Jr., *J. Soc. Ind. Appl. Math.*, **3**, 28 (1955).
16. Seban, R. A., and E. F. McLaughlin, *Intern. J. Heat Mass Transfer*, **6**, 387 (1963).
17. Weissman, M. H., and L. F. Mockros, paper presented at Ann. Conf. Eng. Med. Biol., Boston, Mass. (Nov. 1967).

Manuscript received November 5, 1969; revision received July 8, 1970; paper accepted July 15, 1970. Paper presented at AIChE Houston meeting.